RSC Advances

ROYAL SOCIETY OF CHEMISTRY

www.rsc.org/advances

RSC Advances

RSCPublishing

ARTICLE

Cite this: DOI: 10.1039/x0xx00000x

Asymmetric supercapacitor based on α-MoO_3 cathode and porous activated carbon anode materials

F. Barzegar[a], A. Bello[a], D. Y. Momodu[a], J. K. Dangbegnon[a], F. Taghizadeh[a], M. J. Madito[a], T.M. Masikhwa[a] and N. Manyala[a]*

Received 00th January 2012,
Accepted 00th January 2012

DOI: 10.1039/x0xx00000x

www.rsc.org/

Low cost porous carbon materials were produced from cheap polymer materials and graphene foam materials which were tested as a negative electrode material in an asymmetric cell configuration with α-MoO_3 as a positive electrode. These materials were paired to maximize the specific capacitance and to extend the potential window hence improving on the energy density of the device. The asymmetrical device exhibits significantly higher energy density of 16.75 Wh kg^{-1} and a power density of 325 W kg^{-1}.

Introduction

In the last few decades, there has been a tremendous growth in the development of new hybrid energy storage technology to address the challenges of renewable and sustainable energy sources. Supercapacitors are at the forefront of this research and are recognized as a special type of device for next generation energy storage due to their high power densities and excellent cycling ability, which makes them suitable for use in hybrid electric vehicles, memory backup systems and industrial equipment that relies on long cycle-life times and uninterruptable power supply [1].

Aqueous asymmetric supercapacitors (AASs) are promising hybrid energy storage devices as they have been shown to provide a wider operating voltage at higher energy density compared to symmetric capacitors [2,3] by combining a battery-type electrode Faradaic cathode (transition metal oxide) material and a capacitor-type electrode anode material (usually an activated carbon). AASs make use of the different potential windows in the anode and cathode leading to an increased operational voltage of the aqueous electrolyte [3] and significantly improving the energy density of devices. Generally most AASs ECs make use of activated carbon (AC) as the negative electrode [4,5] because of the anomalous pseudocapacitance mechanism at the surfaces of carbon-based electrodes when scanned at a negative potentials in aqueous electrolytes [6]. For the positive electrode, conductive polymers and various transition metal oxides [7–11] are widely studied due to rapid and reversible electron exchange reactions at the electrode interface which contribute to the high energy and power densities of AASs.

In order to achieve high performance AASs, several AASs systems have been developed for example AC//$Ni(OH)_2$ [12], graphene//$Ni(OH)_2$ [13], carbon nanotubes// MnO_2 [9] and activated carbon(AC)//MoO_3 [14] were all fabricated and exhibited high energy storage capabilities. Nevertheless, the energy capabilities of these devices are still far from commercialization due to the poor capacitive performance of positive electrode materials at the high current loading and the corresponding carbon negative materials in a low utilization [15]. Thus, the synergistic effect in energy storage from positive electrode and power delivery from negative electrode is greatly limited in the asymmetric configuration [15]. The activated carbon(AC)//MoO_3 [14] AAS involves a two-dimensional (2D) material: MoO_3 which is part of the family of phyllosilicates. The interest for this 2D layered material was boosted by the unique properties of graphene. In fact, similar properties to those of graphene are expected for this 2D material. In other words, owing to the exceptional electrochemical performance of graphene, it is conceivable to also expect such performance for MoO_3. Although numerous research has been carried out so far there are still few studies reporting the fabrication of AASs with activated carbon from polymer based materials as the anode and MoO_3 as the cathode in an aqueous electrolyte media. In this work, we report on a design of AASs based on activated carbon with 3D interconnected pores derived from a combination of polymer materials such as polyvinyl alcohol (PVA), polyvinylpyrrolidone (PVP) and graphene foam (GF) on a nickel foam current collector as the anode electrode and using mesoporous MoO_3 nanosheets as cathode electrode material. The hybrid material showed high rate capability compared to a pure MoO_3 electrode. The optimized AAS showed a specific capacitance of 179 F g^{-1} at 0.5 A g^{-1} and a maximum energy density of 16.75 Wh kg^{-1} based on the total mass of active materials operating at a potential window of 1.3 V.

Experimental

Synthesis of electrode materials

Activated carbon was first prepared by the process reported in our previous work [16], while α-MoO_3 prepared by hydrothermal system as recommended by Wang *et al.*[17]. First, ammonium peramolybdate ($(NH_4)_6Mo_7O_{24}\cdot 4H_2O$) and sodium diethyldithiocarbamate ($(C_2H_5)_2NCS_2Na\cdot 3H_2O$) were dissolved in deionized water and magnetically stirred for 12 h and the solution mixture was kept stationary under the ambient condition for another 12 h. The resulting yellow precipitate ($Mo((C_2H_5)_2NCS_2)_2O_2$) was filtered, washed with deionized water and dried at 70 °C for 12 h. After, which the $Mo((C_2H_5)_2NCS_2)_2O_2$ was placed into a Teflon-lined stainless steel autoclave and the deionized water was added with stirring. The autoclave was sealed and maintained at 200 °C for 24 h.

The resulting precipitates was filtered, washed with deionized water and ethanol and dried in vacuum at 100 °C for 6 h. Nanostructured α-MoO_3 was obtained by heating the hydrothermally synthesized powder in air at 370 °C for 6 h.

Microstructural characterization

Nitrogen adsorption–desorption isotherms were measured at −196 °C using a Micromeritics ASAP 2020. All the samples were degassed at 180 °C for more than 12 h under vacuum conditions. The surface area was calculated by the Brunauer–Emmett–Teller (BET) method from the adsorption branch in the relative pressure range (P/P_0) of 0.01 - 0.2. The samples were also characterized using powder X-ray diffraction (XRD). An XPERT-PRO diffractometer (PANalytical BV, Netherlands) with theta/theta geometry, operating a cobalt tube at 35 kV and 50 mA, was used. The XRD patterns of all specimens were recorded in the 10.0^0 – 80.0^0 2θ range with a counting time of 5.240 seconds per step. The SEM images were obtained on a Zeiss Ultra Plus 55 field emission scanning electron microscope (FE-SEM) operated at an accelerating voltage of 2.0 kV.

Electrochemical characterization

All electrochemical measurements were carried out using a Bio-logic SP-300 potentiostat such as cyclic voltammetry (CV), chronopotentiometry (CP) and electrochemical impedance spectroscopy (EIS). The negative electrode was prepared by mixing the active material (AC), and polyvinylidene fluoride (PVDF) binder with a weight ratio of 9:1 which was homogenized and dispersed in N-methylpyrrolidone (NMP) solution, and the slurry was then uniformly pasted on a nickel foam current collector and dried at 60^0 C in an oven for 8 hours to ensure complete evaporation of the NMP. The positive electrode was made by mixing the active material (α-MoO_3), polyvinylidene fluoride (PVDF) binder and carbon black (CB) to improve the conductivity of material with a weight ratio of 8:1:1 and dispersed in N-methylpyrrolidone (NMP) solution, and the slurry was then uniformly pasted on a nickel foam current collector and dried at 60 ^{o}C in an oven for 8 hours. The electrochemical test of the asymmetric cell was carried out in a two electrode cell configuration by means of coin-type cells with thickness of 0.2 mm and diameter of 16 mm, using a glass microfiber filter paper as the separator in 6 M KOH aqueous electrolyte solution. The three electrode measurements were performed for both AC and α-MoO_3 as the working electrodes, glassy carbon plate as the counter electrode and Ag/AgCl (3 M KCl) serving as the reference. The specific capacitance (C_s) can be calculated from CV curves according to the following equation [18]:

$$C_S = \frac{\int I\, dU}{vm\Delta U} \quad (1)$$

or C_s can be calculated from charge–discharge curves according to the equation [18]:

$$C_S = \frac{I\,\Delta t}{m\,\Delta U} \quad (2)$$

Where I is the current, ΔU is the potential window, v is the sweep rate (mV s^{-1}), m is the mass of total electrode active materials and Δt is the discharge time. The energy density (E (Wh kg^{-1})) and power density (P (W kg^{-1})) of EC_s can be then calculated from C_s according to the following equations:

$$E = \frac{1}{2} C_S \Delta U^2 = \frac{1000 \times C_s \times \Delta U^2}{2 \times 4 \times 3600} = \frac{C_s \times \Delta U^2}{28.8} \quad (3)$$

$$P = \frac{E}{t} = \frac{3600 \times E}{1000 \times \Delta t} = \frac{3.6 \times E}{\Delta t} \quad (4)$$

In construction of an asymmetric ECs, the voltage split is dependent on the capacitance of the active material in each electrode. Therefore, it is very important to take care of the mass balancing of each electrode by taking into account the charge equality: $Q_+ = Q_-$, where Q_+ and Q_- are the charges stored in the positive and negative electrodes, respectively. The charge can be expressed by [19]:

$$Q = C_s M \Delta U \quad (5)$$

where C_s is the specific capacitance of active material, M is the mass of each active material and ΔU is the potential range during charge-discharge process. In order to get $Q_+ = Q_-$, the mass balancing will follow the equation:

$$\frac{M_+}{M_-} = \frac{C_{s-}\,\Delta U_-}{C_{s+}\,\Delta U_+} \quad (6)$$

Results and discussion

Figure 1 (a) and (b) represent the BET results of MoO_3 and AC materials respectively. The nitrogen adsorption and desorption isotherm shows type 3 characteristics for MoO_3 and type 1 characteristics for AC. The corresponding specific surface area of MoO_3 is approximately 5.5 m^2 g^{-1} and for Ac is about 2923 m^2 g^{-1}. Moreover, the pores constructed in MoO_3 are mainly mesopore structure (inset to Figure 1 (a)) and in AC are mainly micropore structure with a broad pore size distribution of 2 - 7 nm and an average pore size of 2.7 nm (inset to Figure 1 (b)).

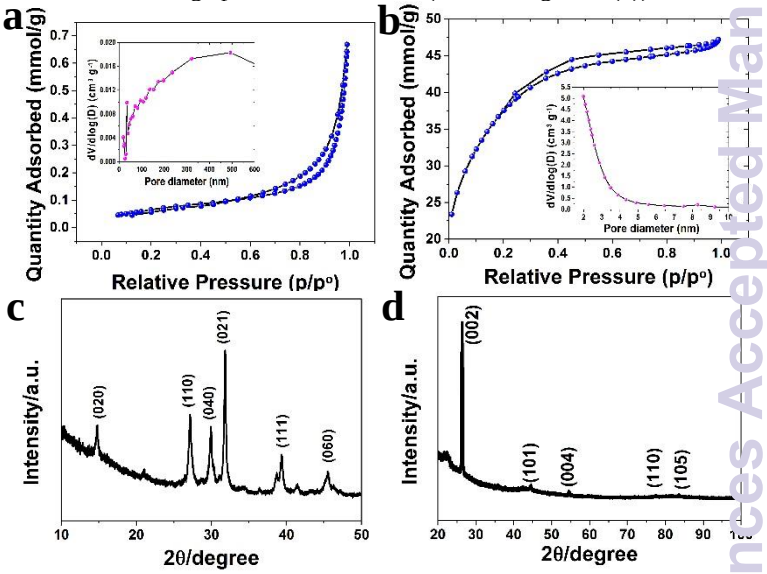

Figure 1. (a) and (b) the N_2 adsorption-desorption isotherm of the α-MoO_3 and AC respectively (insets show pore size distribution), (c) and (d) the X-ray diffraction of the α-MoO_3 and AC respectively

Figure 1 (c) represents the XRD patterns of MoO_3 powder. The wavelength used for the XRD analysis was Co-K_α, 1·7890 Å. After the synthesis, it was found that the peaks corresponding to (0 2 0), (1 1 0), (0 4 0), (0 2 1), (1 1 1), (0 6 0) planes are of orthorhombic crystal structure of MoO_3 [20,21]. It is noted that all the XRD peaks are identified to be MoO_3 peaks (COD: 96-900-9670) which crystallizes in the orthorhombic system with space group Pbnm (62), and lattice parameters a= 3.9616 Å, b= 13.8560 Å, c= 3.6978 Å. The (020) peaks were clearly detected, and indicated the presence of orthorhombic phase rather than the monoclinic. From lattice parameters we can identify the phase of the MoO_3 to be α-phase (see Figure 2). Figure 1 (d) represents the XRD patterns of AC powder. The wavelength used for the XRD analysis was Cu-K_α, 1·5405 Å. It is noted that all the XRD peaks are identified to Graphite peaks (COD: 96-900-8570) which crystallizes in the orthorhombic system with space group P63mc(186), lattice parameters a= 2.4560 Å and c= 6.6960 Å.

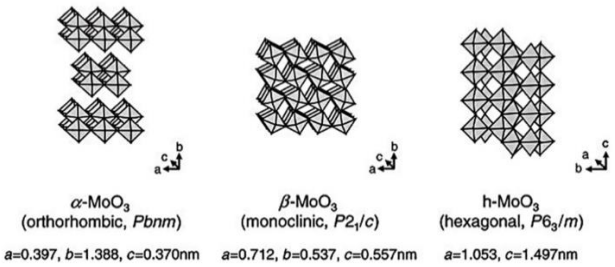

Figure 2. Illustrations of three MoO_3 crystal structures of α, β, and h phases [22]

Figure 3 (a) and (b) show the low and high magnification SEM of the α-MoO_3. It can be seen from these Figure that the α-MoO_3 comprises clusters of interleaving nano-platelets, whose thicknesses range from 20 to 85 nm. Figure 3 (c) and (d) present the low and high magnification SEM of the AC. As observed, the porosity of this AC is very high hence making it suitable for large ion-accessible surface for fast ion transport in high performance supercapacitors.

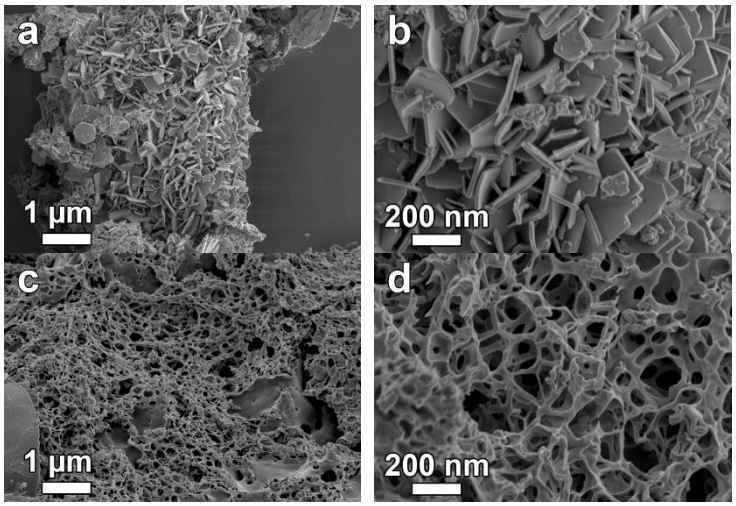

Figure 3. Low and high magnification SEM image of (a) and (b) α-MoO_3 (c) and (d) AC

To evaluate the electrochemical properties and quantify the specific capacitance of the as-prepared AC and α-MoO_3, we performed cyclic voltammetry (CV) measurements on these two electrode materials in a 6M KOH aqueous solution using a three electrode system (Figure 4). The CV for AC electrode was measured within a potential window of -0.8 to 0.0 V and for α-MoO_3 was measured within a potential window of 0.0 to 0.5 V vs Ag/AgCl at a scan rate of 10 mV s^{-1}. The detailed three electrode electrochemical measurements of each single electrode are documented in Figures S1 and S2 in the supporting information. From the CV curve (Figure 4) of AC electrode, no peaks of oxidation and reduction are observed, indicating a typical characteristic of EDL capacitor behavior, while the CV shape of the α-MoO_3 electrode in the potential range of 0.0 to 0.5 V is of pseodocapacitance type showing oxidation and reduction peaks.

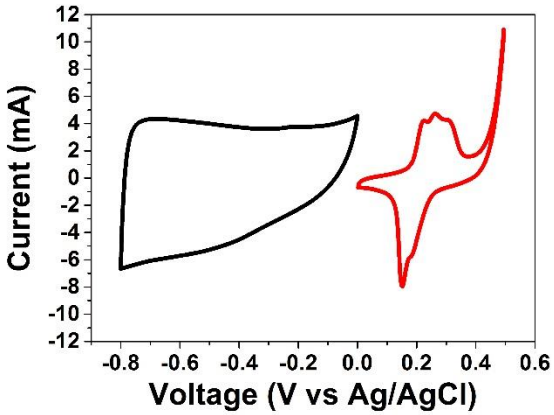

Figure 4. CV curves of α-MoO_3 (red curve) and AC (black curve) electrodes performed in three electrode system in 6M KOH solution at a scan rate of 10 mV s^{-1}

On the basis of these results, it is expected that the operating cell voltage could be extended to about 1.3 V in 6M KOH solutions as electrolyte if the α-MoO_3 electrode as a cathode and the AC electrode as an anode are assembled into asymmetric ECs (Figure 5).

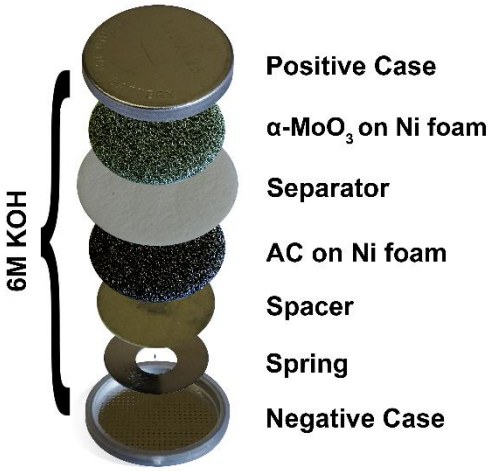

Figure 5. Schematic of the assembled structure of asymmetric ECs based on α-MoO_3 as positive electrode and AC as negative electrode

For making two electrode cell, according to equation 6, the mass of the MoO_3 should be two times mass of the AC ($\frac{M_{\alpha-MoO3}}{M_{AC}} = 2$). Figure 6 (a) shows a typical CV of the asymmetric EC at scan rates from 5 to 100 m Vs^{-1} in a potential window of 1.3 V. The mirror image shape of the CV indicates excellent reversible reaction at the electrode/electrolyte interface [23]. An asymmetric charge/discharge curve showing EDLCs with little pseudocapacitive behavior at all current densities (Figure 6 (b)) were observed. The specific capacitance of the MoO_3/AC can reach 179 F g^{-1} at a scan rate of 0.5 Ag^{-1}. The Ragone plot and the specific capacitance as function of the current density of the asymmetric device are shown in Figure 6 (c). The specific capacitance decreases from 179 F g^{-1} to 37 F g^{-1} with increasing current density from 0.5 to 10 A g^{-1}. The maximum energy density of the device was recorded as 16.75 Wh kg^{-1} and power density of 325 W Kg^{-1} at a current density of 0.5 A g^{-1}. The energy density is higher than those reported

symmetric and asymmetric supercapacitor such as MoO_3/MWCNTs//MoO_3/MWCNTs (7.28 Wh kg^{-1}) [24], $Ni(OH)_2$/UGF//a-MEGO (13.4 wh kg^{-1}) [25] but smaller than those reported for $GrMnO_2$//$GrMoO_3$ (42.6 Wh kg^{-1}) [26] and PANI//MoO_3 (71.9 Wh kg^{-1}) [27]. Nevertheless, our electrode material presents better stability compared to $GrMnO_2$//$GrMoO_3$ and PANI//MoO_3 materials. The latter already degrading after 200 cycles.

As shown in Figure 6 (d), the AASs cell shows no capacitance loss after 10000 cycles at current density of 2 A g^{-1}. However, a small increase in the capacitance (~1.13 %) was observed after the initial cycling process which is similar to what was observed by Ren et .al [28] and this was tentatively attributed to the swelling of the carbon material at some defective sites, promoting electrolyte ions to intercalate into the space created by the swelling or creation of more pores after many CD cycles and leading to more accessible surface area and hence increase in the efficiency of the cell which was stable and maintained throughout the cycling process. [28].

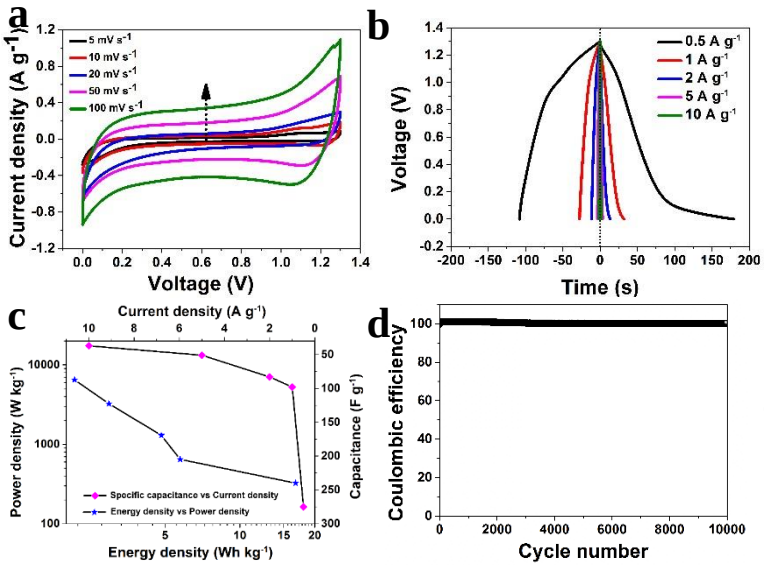

Figure 6. (a) CV curves at scan rates of 5 to 100 mV s^{-1}, (b) the galvanostatic charge/discharge curves from 0.5 to 10 A g^{-1} current densities, (c) Ragone plot and the specific capacitance as function of the current density and (d) Cycle stability at a constant current density of 2 A g^{-1} of asymmetric cell of α-MoO_3/AC

EIS is an important parameter for investigating the electrical conductivity of electrodes. We measured the impedance of the electrode materials in the frequency range of 0.01 to 10^5 Hz.

The intercept on the x-axis of the Nyquist plot (Figure 7 (a) and (b)) in the high-frequency region represents the electronic resistance of the device, also known as the equivalent series resistance (ESR), denoted as R_S. The semicircle is a result of the charging of the double layer of the activated carbon (Figure 7 (b)). The charge transfer resistance (R_{CT}) and the double-layer capacitance C_{DL} lie in the high-frequency to mid-frequency region. The Nyquist plot shows a nearly vertical line in the low-frequency region representing the diffusion of ions to the interface between electrode and electrolyte. The deviation from the ideal vertical behavior is attributed to the presence of resistance with a Warburg impedance characteristic element denoted by W, which is expressed as $A/(j\omega)^{0.5}$ [29], where A is the Warburg coefficient, ω is the angular frequency.

The circuits used for fitting of the EIS experimental data of the Nyquist plot for each electrode material was performed with a fitting program ZFIT/EC-Lab version 10.38 and are represented in the inset to Figure 7 (a) and (b) for MoO_3 and AC respectively. In Figure7 (a) the equivalent circuits, has a solution resistance (R_S) connected in series with a constant phase element (CPE_{DL}), and the CPE_{DL} is connected in parallel with the charge-transfer resistance (R_{CT}) and the mass capacitance (CPE_L), while the Warburg element (W) and the leakage current R_L are all in series with R_S. Figure 7 (b) CPE_{DL}, CPE_L, and R_{CT} are all parallel to each other and are in series with the R_S which is also in series with both the R_L and W. CPE_{DL} representing the double-layer capacitance related to the porous electrode. CPE_L represents the ideal polarizable capacitance that would give rise to a straight line parallel to the imaginary axis. The deviation from the ideal situation suggests that a resistive element R_L is associated with CPE_L. The impedance of CPE_{DL} is defined as $Z_{CPE} = T(j\omega)^{-n}$ [30], where T and n are frequency-independent constants and ω is the angular frequency. The n is a correction factor which is related to the capacitive kinetics and roughness of electrode surfaces. The values for n range between 0 and 1: n = 1 denotes that the CPE element is an ideal capacitor, for n = -1, CPE behaves as an inductor, while n = 0 and 0.5 denote a resistance and Warburg behaviors respectively [30]. Figure 7 (c) presents the Nyquist plot of the asymmetric device fabricated with ESR value of 0.39 Ohms while Figure 7 (d) shows the fitting which combine the two sets of fitting parameters listed in Tables S1 and S3 in the supporting information for a single electrodes in series. The fittings show that the impedance spectra of the electrodes fit perfectly with the experimental data without further adjustments. The Nyquist plot before and after cycling is shown in Figure 7 (e).

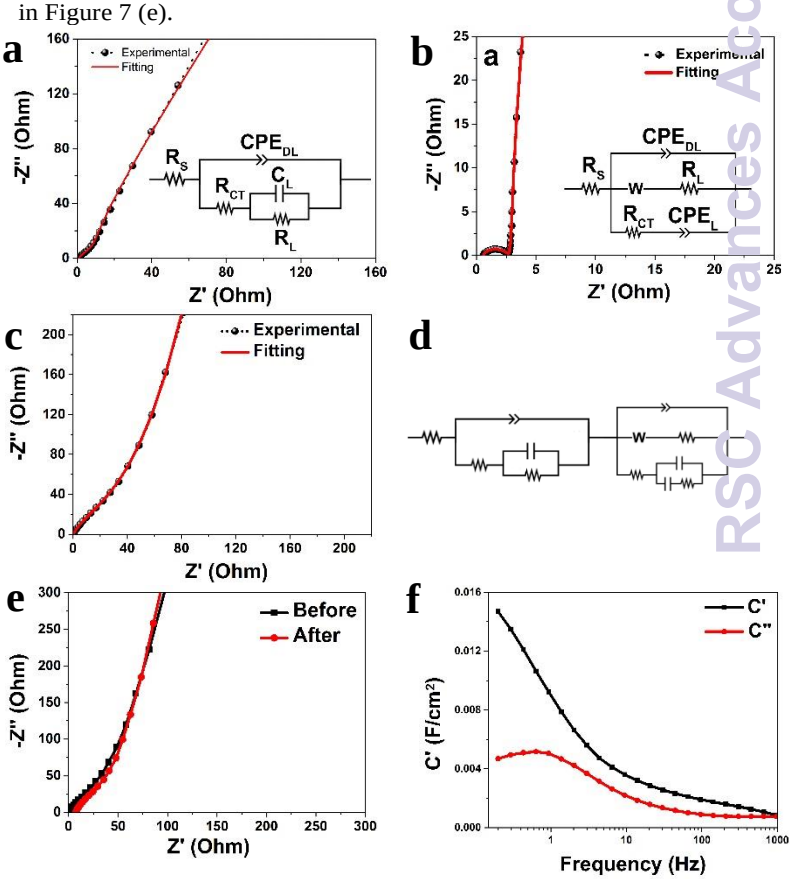

Figure 7. (a) and (b) EIS plot and fitting curve for single electrode with the insets to the Figure being equivalent circuits used for fitting the data of the α-MoO_3 and AC respectively, (c) EIS plot and fitting curve for the asymmetric cell, (d) equivalent circuit used for fitting the asymmetric cell data in (c), (e) EIS before and after cycling, (f) the real and the imaginary part of the cells capacitance against frequency.

The supercapacitors behave as a series combination of a resistance and capacitance and both of them depend on the frequency. In the low frequency region, the capacitance ($C(\omega)$) can be defined as the combination of imaginary part of the capacitance ($C''(\omega)$) and real part of the capacitance ($C'(\omega)$), and they can be expressed by the following equations [31,32]:

$$C(\omega) = C'(\omega) + jC''(\omega) \quad (7)$$

$$C'(\omega) = -\frac{Z''(\omega)}{\omega|Z(\omega)^2|} \quad (8)$$

$$C''(\omega) = -\frac{Z'(\omega)}{\omega|Z(\omega)^2|} \quad (9)$$

where $C'(\omega)$ corresponds to the static capacitance which is tested during the constant current discharge, $C''(\omega)$ corresponds to energy dissipation of the supercapacitor by IR drop and an irreversible faradic charge transfer process, which can cause the hysteresis of the electrochemical processes. $|Z(\omega)|$ is the impedance modulus, and **ω** is the angular frequency [31,32]. Based on the above formulae, the capacitance (C') of the cell is 0.015 F (from topmost part of the C' graph) as shown in Figure 7 (f), C'' define the transition frequency between a pure capacitive and a pure resistive behavior of the AASs with a relaxation time of ~1.7 s obtained by taking the reciprocal of the maximum frequency in the C'' graph (Figure 7 f). These values show that the cells can be fully discharged within a very short time with an efficiency of more than 50 % [30].

Conclusions

We have successfully fabricated an asymmetric supercapacitor device based on porous activated carbon material as negative electrodes and α-MoO3 as positive electrode. The asymmetrical device shows high specific capacitance of 179 F g^{-1}, energy density of 16.75 Wh kg^{-1}, power density of 325 W Kg^{-1} and good stability after 10000 cycles at an operating voltage of about 1.3 V in 6 M KOH aqueous electrolytes. It shows that pairing such hybrid material could be an excellent approach to produce supercapacitors with high energy and power densities. These encouraging results could open up new possibility of three dimensional porous carbons based on cheap polymer materials and graphene foam for applications in asymmetric supercapacitors with high potential window, high energy and high power densities to meet the increasing energy demand of the global society.

Acknowledgements

This work is based on research supported by the South African Research Chairs Initiative (SARChi) in Carbon Technology and Materials of the Department of Science and Technology (DST) and the National Research Foundation (NRF). Any opinion, findings and conclusions or recommendations expressed in this work are those of authors and therefore the NRF and the DST do not accept any liability with regard thereto. F. Barzegar and D. Y. Momodu acknowledge financial support from the University of Pretoria and the NRF for their PhD bursaries, while A. Bello acknowledge the University of Pretoria's financial support for their postdoctoral fellowships.

Notes and references

[a]*Department of Physics, Institute of Applied Materials, SARCHI Chair in Carbon Technology and Materials, University of Pretoria, Pretoria 0028, South Africa.*

[*]***Email address**: ncholu.manyala@up.ac.za (N. Manyala)*

***Corresponding author** Tel: +27 (0)12 420 3549, Fax: +27 (0)12 420 2516*

Electronic Supplementary Information (ESI) available: [Fitting parameters for the single electrodes and electrochemical characterization of three electrode system for each electrode]. See DOI: 10.1039/b000000x/

1 B. E. Conway, *Electrochemical Supercapacitors: Scientific Fundamentals and Technological Applications*, Kluwer Academic/Plenum, New York, 1999.

2 J. W. Long, D. Bélanger, T. Brousse, W. Sugimoto, M. B. Sassin and O. Crosnier, *MRS Bull.*, 2011, **36**, 513–522.

3 K. Naoi, S. Ishimoto, J. Miyamoto and W. Naoi, *Energy Environ. Sci.*, 2012, **5**, 9363.

4 Y. Zhai, Y. Dou, D. Zhao, P. F. Fulvio, R. T. Mayes and S. Dai, *Adv. Mater.*, 2011, **23**, 4828–50.

5 N. W. Duffy, W. Baldsing and A. G. Pandolfo, *Electrochim. Acta*, 2008, **54**, 535–539.

6 F. Béguin, K. Kierzek, M. Friebe, A. Jankowska, J. Machnikowski, K. Jurewicz and E. Frackowiak, *Electrochim. Acta*, 2006, **51**, 2161–2167.

7 Z. Algharaibeh, X. Liu and P. G. Pickup, *J. Power Sources*, 2009, **187**, 640–643.

8 V. Khomenko, E. Raymundo-Piñero and F. Béguin, *J. Power Sources*, 2006, **153**, 183–190.

9 H. Jiang, C. Li, T. Sun and J. Ma, *Nanoscale*, 2012, **4**, 807–12.

10 Y. Cheng, S. Lu, H. Zhang, C. V Varanasi and J. Liu, *Nano Lett.*, 2012, **12**, 4206–11.

11 X. Liu, R. Ma, Y. Bando and T. Sasaki, *Adv. Mater.*, 2012, **24**, 2148–53.

12 S. Nohara, T. Asahina, H. Wada, N. Furukawa, H. Inoue, N. Sugoh, H. Iwasaki and C. Iwakura, *J. Power Sources*, 2006, **157**, 605–609.

13 J. Yan, Z. Fan, W. Sun, G. Ning, T. Wei, Q. Zhang, R. Zhang, L. Zhi and F. Wei, *Adv. Funct. Mater.*, 2012, **22**, 2632–2641.

14 W. Tang, L. Liu, S. Tian, L. Li, Y. Yue, Y. Wu and K. Zhu, *Chem. Commun. (Camb).*, 2011, **47**, 10058–60.

15 R. Wang and X. Yan, *Sci. Rep.*, 2014, **4**, 3712.

16 A. Bello, F. Barzegar, D. Momodu, J. Dangbegnon, F. Taghizadeh and N. Manyala, *Electrochim. Acta*, 2015, **151**, 386–392.

17 T. Wang, J. Li and G. Zhao, *Powder Technol.*, 2014, **253**, 347–351.

18 W. Zhang, C. Ma, J. Fang, J. Cheng, X. Zhang, S. Dong and L. Zhang, *RSC Adv.*, 2013, **3**, 2483.

19 A. Bello, F. Barzegar, D. Momodu, J. Dangbegnon, F. Taghizadeh, M. Fabiane and N. Manyala, *J. Power Sources*, 2015, **273**, 305–311.

20 T. Mizushima, K. Fukushima, H. Ohkita and N. Kakuta, *Appl. Catal. A Gen.*, 2007, **326**, 106–112.

21 A. Ganguly and R. George, *Bull. Mater. Sci.*, 2007, **30**, 183–185.

22 K. Koike, R. Wada, S. Yagi, Y. Harada, S. Sasa and M. Yano, *Jpn. J. Appl. Phys.*, 2014, **53**, 05FJ02.

23 Z.-S. Wu, W. Ren, D.-W. Wang, F. Li, B. Liu and H.-M. Cheng, *ACS Nano*, 2010, **4**, 5835–42.

24 L. S. Aravinda, U. Bhat and B. Ramachandra Bhat, *Electrochim. Acta*, 2013, **112**, 663–669.

25 J. Ji, L. L. Zhang, H. Ji, Y. Li, X. Zhao, X. Bai, X. Fan, F. Zhang and R. S. Ruoff, *ACS Nano*, 2013, **7**, 6237–6243.

26 J. Chang, M. Jin, F. Yao, T. H. Kim, V. T. Le, H. Yue, F. Gunes, B. Li, A. Ghosh, S. Xie and Y. H. Lee, *Adv. Funct. Mater.*, 2013, **23**, 5074–5083.

27 H. Peng, G. Ma, J. Mu, K. Sun and Z. Lei, *J. Mater. Chem. A*, 2014, **2**, 10384.

28 G. Ren, X. Pan, S. Bayne and Z. Fan, *Carbon N. Y.*, 2014, **71**, 94–101.

29 Y. Zhou, H. Xu, N. Lachman, M. Ghaffari, S. Wu, Y. Liu, A. Ugur, K. K. Gleason, B. L. Wardle and Q. M. Zhang, *Nano Energy*, 2014, **9**, 176–185.

30 D. Pech, M. Brunet, H. Durou, P. Huang, V. Mochalin, Y. Gogotsi, P.-L. Taberna and P. Simon, *Nat. Nanotechnol.*, 2010, **5**, 651–4.

31 X. Zhang, X. Wang, L. Jiang, H. Wu, C. Wu and J. Su, *J. Power Sources*, 2012, **216**, 290–296.

32 P. L. Taberna, P. Simon and J. F. Fauvarque, *J. Electrochem. Soc.*, 2003, **150**, A292.

